He Mingjun (Orcid ID: 0000-0002-7731-1929)
Bartley Evan (Orcid ID: 0000-0002-2773-7331)
Christakos George (Orcid ID: 0000-0002-1865-5764)

Accepted Article

Space-Time Characterization and Risk Assessment of Nutrient Pollutant Concentrations in China's Near Seas

Qutu Jiang[1], Junyu He[1], Jiaping Wu[1], Mingjun He[1], Evan Bartley[2], Guanqiong Ye[1*], George Christakos[1, 2*]

1 Ocean College, Zhejiang University, Zhoushan 316021, China
2 Department of Geography, San Diego State University, San Diego, CA 92182, USA

* Corresponding authors: Guanqiong Ye (gqy@zju.edu.cn); George Christakos (gchrista@sdsu.edu)

Key Points:

- Bayesian maximum entropy maps showed that nitrate and phosphate concentrations had similar spatial distributions.
- Nitrate and phosphate distributions exhibited different seasonal patterns that may have been affected by coastal hydrodynamics and human activities.
- Stochastic site indicators showed that nitrate pollution was much more serious than phosphate pollution.

This article has been accepted for publication and undergone full peer review but has not been through the copyediting, typesetting, pagination and proofreading process which may lead to differences between this version and the Version of Record. Please cite this article as doi: 10.1029/2019JC015038

© 2019 American Geophysical Union. All rights reserved.

Abstract: Human activities interacting with coastal waters lead to large amounts of nutrient loading and severe water pollution in China's near Seas. In this context, a comprehensive quantitative characterization of the spatiotemporal variation of nutrient pollutant concentrations is a key component of any reliable seawater quality assessment and integrated coastal management plan. The present work combines the Bayesian maximum entropy method with stochastic site indicators to estimate monthly nitrate and phosphate concentrations in China's near Seas during 2015, explore their spatiotemporal variation, and provide an explicit quantitative assessment of seawater quality in conditions of in situ uncertainty. This makes it the first study of space-time nutrient pollutant characterization at a national-scale in a coastal seawater environment. The results showed that nitrate and phosphate distributions exhibit the same spatial trends along China's near Seas, whereas high nutrient pollution levels are found in the Yangtze river, Liaohe river and Pearl river estuaries. Local differences of temporal trends exist between nitrate and phosphate distributions, which suggest that distinct remediation strategies are needed to properly satisfy the required seawater quality standards. The average nitrate and phosphate concentrations across space-time were found to be equal to 0.271 and 0.015 *mg/L*, respectively. The nitrate and phosphate concentrations exceeding the 4th grade seawater quality standard during 2015 were about 11% and 2.6%, respectively. The study of both the seasonal changes in human activities along the coastal cities and the temporal marine hydrodynamics can offer a better understanding of seawater quality and the biogeochemical process of nutrient transport and distribution.

Keywords: Nutrient pollutants, China's near seas, Bayesian maximum entropy, stochastic site indicators.

1. Introduction

With the rapid economic development and growing population in China's coastal cities, various anthropogenic activities have led to substantially increased nutrient inputs to coastal waters from different sources, such as agricultural fertilizer usage, domestic/industrial wastewater and aquaculture (Qu et al. 2010; Strokal et al. 2014; Wang et al. 2018). Nutrients are very important to marine primary productivity and marine environmental health. Excessive nutrient discharge (especially nitrate and phosphate) to coastal waters can cause adverse ecological effects, such as loss of habitat and biodiversity (Diaz and Rosenberg 2008), harmful algal blooms (Li et al. 2014), hypoxia (Breitburg et al. 2018) and ocean acidification (Cai et al. 2011), thereby affecting marine ecosystem health and sustainable coastal development (Howarth et al. 2006; Smith 2006; Conley et al. 2009). Thus, comprehensive monitoring, assessment and management of these marine pollutants are of great significance and have received much attention by scientific researchers and policy makers in recent decades (Huang et al. 2013; Kitsiou and Karydis 2011; Khangaonkar et al. 2018; Yu et al. 2019).

Several statistical techniques have been used to study nutrient pollutant distributions, such as principal component analysis, cluster analysis and regression analysis (Primpas et al. 2010; Lundberg et al. 2009; Everaert et al. 2017). These statistical techniques rely mainly on sparsely distributed samples and/or ignore spatial autocorrelation and heterogeneity. Geostatistical techniques, on the other hand, generate unbiased and optimal estimates of the pollutant distributions that account for spatial nutrient pollutant correlations in the area of interest (Christakos 2000). Many studies have employed geostatistical techniques to model field data in aquatic environments. Murphy et al. (2010) compared different spatial interpolation methods for water quality evaluation in the Chesapeake Bay, and the results indicated that kriging techniques generally outperform inverse distance weighting techniques for all parameters and depths. Zhou et al. (2013) used universal kriging to estimate the extent of hypoxia in Lake Erie, and to map the spatial distribution of dissolved oxygen with auxiliary variables such as bathymetry and longitude. Ren et al. (2016) utilized the mean of surface (MSN) technique to assess the mean concentrations of nitrate and phosphate in the Yangtze estuary, taking regional heterogeneity into account. Most of these studies were concerned with small-scale aquatic ecosystems, such as a special estuary or a coastal sea region, where the human activity intensity and pollution sources differ between geographical regions. Moreover, these studies focused primarily on spatial pollutant estimation, and ignored the direct consideration of temporal covariance and dynamics (these issues were considered separately as supplements to spatial estimation and pollution status assessment). Apart from the human factor, nutrient concentrations are affected by changing hydrologic and meteorological conditions (e.g., upwelling, current drift, and precipitation), which may lead to seasonal adverse incidences such as hypoxia and harmful algal blooms when pollutant concentrations reach a certain threshold under specific aquatic ecosystem conditions. Therefore, the

© 2019 American Geophysical Union. All rights reserved.

determination of the spatiotemporal pollutant trends can provide valuable information on how marine ecosystems respond to changing pollutant concentrations, thus allowing for timely warnings and marine spatial planning, as well as the implementation of conservation measures for marine environmental health assessment purposes.

The present work provides, for the first time, a spatiotemporal nutrient pollutant characterization of the coastal seawater environment at the national-scale. Since China's reform and opening up to the outside world in 1978, China's GDP grew 75 times between 1978 and 2016. Rapid economic and social development has led to increased nutrient loading, which has been associated with 1392 harmful algal bloom events in China during the period 2000-2017 (Wang et al. 2018). Since the "Marine Ecological Civilization Construction" policy in China puts great emphasis on marine ecological restoration and environmental protection, the comprehensive characterization and assessment of the marine ecological state provides very important information to policy makers and researchers seeking to manage pollution sources and develop effective remediation strategies. A total of 3962 monthly surface water samples collected during 2015 were included in this study, whose goals were threefold: (1) Use the Bayesian maximum entropy (BME) method to represent the space-time nitrate and phosphate concentration distributions in China's near Seas and generate monthly nutrient pollutant predictions across space (maps); (2) explore the seasonal variability of the space-time nutrient distributions based on these predictions; and (3) use stochastic site indicators (SSI) to quantify the uncertainty and assess the risk associated with the nutrient pollutant variations for sustainable development and management purposes. The results of this work provide a comprehensive spatiotemporal characterization and assessment of the nitrate and phosphate distributions throughout China's coastal Seas that could contribute to the development of effective remediation plans and the scientific management of nutrient pollution in these waters.

2. Materials and Methods

2.1 Study domain and data

The study area is located along China's near Seas, including the Bohai Gulf, the Yellow Sea, the East China Sea and the South China Sea. Its geographical boundaries are determined according to administrative divisions (including internal seawaters and twelve nautical miles territorial seas), where most of the monitoring sites are located (Fig 1). The East and South China Seas receive large amounts of nutrient pollutants from rivers, especially from the Yangtze River, the Yellow River (Fig S1) and the Pearl River, where there are large drainage areas and intense anthropogenic activities (especially those related to industrial and agricultural production; Qu et al. 2010, Strokal et al. 2014). The period considered in this work is the year 2015. Accordingly, the space-time domain of interest can be symbolically presented as

$$D=(A,T),$$

where A = geographical area along China's near Seas and T = year 2015. The annual frequency and area of harmful algal blooms along Chinese Seas increased rapidly in the 21st century and peaked in the mid-2000s (Wang et al., 2018).

We used a total of 3962 monthly surface samples that were obtained by the State Oceanic Administration during 2015 (this administration has been recently integrated in to the Ministry of Natural Resources of People's Republic of China, http://www.mnr.gov.cn). The monitoring parameters cover a range of variables describing coastal water quality such as nitrate (N), phosphate (P), pH, dissolved oxygen (DO) and chemical oxygen demand (COD). The methods used for parameter concentration assessment purposes followed the national marine monitoring standards (GB17378-2007; https://www.nmemc.org.cn/). There are a total of 652, 977, 1187 and 1146 regional monitoring samples at Bohai Sea (BS), Yellow Sea (YS), East China Sea (ECS) and South China Sea (SCS), respectively. For each year, most of the field sampling work was conducted during the months of March, May, August and October, but several more samples were collected during the other months as well (Fig S2). These sites (latitude, longitude) were converted to Mercator, and the final monthly nitrate and phosphate concentration predictions were generated on a $5km^2$ grid.

2.2 Space-time estimation and mapping using BME

© 2019 American Geophysical Union. All rights reserved.

The space-time prediction of nitrate and phosphate concentrations was based on the BME theory (Christakos 2000), which has been applied successfully in various fields, including water quality, air pollution and epidemiology (e.g., Coulliette et al. 2009, Fei et al. 2016, Jiang et al. 2019). In the BME modeling context, let $NP(\boldsymbol{p})$ be the spatiotemporal random field model (S/TRF, Christakos 2017) representing nutrient (nitrate or phosphate) pollutant concentrations in China's near Seas during 2015, where the vector $\boldsymbol{p}=(\boldsymbol{s},t)$ determines a point within the space-time domain D, with $\boldsymbol{s}$ denoting geographical location and t time. To obtain the probability density function (pdf) of possible $NP(\boldsymbol{p})$ values at each space-time point $\boldsymbol{p}$, the BME integrates two major knowledge bases (KB): the core or general *G*-KB that includes the theoretical mean and covariance models of the nitrate and phosphate distributions, and the site-specific *S*-KB that consists of monthly surface samples of nitrate and phosphate concentrations. Notice that BME can incorporate several other information sources, when they are available, e.g., the *G*-KB may include scientific theories and physical laws, and the *S*-KB may include hard (or exact) data, empirical evidence and soft (or uncertain) measurements of various kinds (see, review by He and Kolovos 2018). The fundamental BME equations (Christakos 1990, 2000; Text S2) integrate the *G*-KB with the *S*-KB (i.e., $K=G\cup S$), thus providing a complete probabilistic characterization of the space-time nutrient pollutant distribution in terms of the nutrient pdf $f_K(NP)$ at each point $\boldsymbol{p}$ of interest. The *Spatiotemporal Epistemic Knowledge Synthesis Graphical User Interface* software library (SEKS-GUI, Yu et al., 2007) was used for the computational implementation of BME-based nutrient pollution modeling and mapping.

2.3 Stochastic site indicators (SSI)

The SSI is a set of quantitative indicators that express different yet complementary assessments of over-pollution (i.e., cases where the pollutant exceeding the specified threshold ζ) in the space-time domain of interest. Specifically, the SSI can (*a*) describe a polluted region in terms of its key features (e.g., areal fraction of the over-polluted region, mean over-polluting concentration, spatiotemporal connectivity between over-polluting concentrations), (*b*) indentify regions at risk, and (*c*) reduce uncertainties across broad spatial and temporal scales. The SSI have been shown to be useful tools to characterize and quantify the morphology and evolution of the pollutant distribution of interest (Christakos and Hristopulos 1996a-b, Yang and Christakos 2015, Jiang et al., 2018, He et al., 2019). In this study, a space-time binary random field associated with the nutrient pollutant $NP(\boldsymbol{p})$ is defined as $I_{NP}(\boldsymbol{p},\zeta)=1$ if $NP(\boldsymbol{p})\geq\zeta$, and $=0$ otherwise, where ζ is a threshold expressing the permissible range of nitrate or phosphate concentrations (specified by experts, researchers, or authorities, depending on the case). The $I_{NP}(\boldsymbol{p},\zeta)$ provides a characterization of the excess nutrient pollutant in the space-time domain D of interest under conditions of in-situ uncertainty. Accordingly, the SSI-based nutrient pollutant characterization involves the S/TRF pair

$$\{NP(\boldsymbol{p}), I_{NP}(\boldsymbol{p},\zeta)\},$$

where the $NP(\boldsymbol{p})$ is a function of $\boldsymbol{p}$, whereas the $I_{NP}(\boldsymbol{p},\zeta)$ is a function of both $\boldsymbol{p}$ and ζ.

Sets of one-point ($\boldsymbol{p}$) and two-point ($\boldsymbol{p}$, $\boldsymbol{p}'$) SSI can be derived by considering the polluted sub-domain Θ of the original domain D according to the ζ-thresholds of the nitrate and phosphate concentrations $NP(\boldsymbol{p})$. In mathematical terms, the polluted sub-domain is expressed as

$$\Theta=\{\boldsymbol{p}:\ NP(\boldsymbol{p})\geq\zeta \text{ or } I_{NP}(\boldsymbol{p},\zeta)=1\}\subseteq D.$$

Note that $\zeta=0$ implies that $\Theta\equiv D$, as is intuitively expected. The one-point SSI are functions of the threshold ζ and can be used to evaluate different kinds of ζ-exceeding global nutrient pollutant averages. Yet, the one-point SSI do not describe the space-time dependency (connectivity) of pollutant values, which is what the two-point SSI do. The two-point SSI are functions of both the ζ and the space-time lag $\delta\boldsymbol{p}=\boldsymbol{p}'-\boldsymbol{p}$ between the points $\boldsymbol{p}$ and $\boldsymbol{p}'$. A list of SSI selected for the purposes of the present study are presented in Figs 2b-c. The fundamental SSI operator is

$$A_\Omega^Q[\cdot]=|Q|^{-1}\int_\Omega d\boldsymbol{p}[\cdot],$$

© 2019 American Geophysical Union. All rights reserved.

where Q and Ω express any of the regions D, Θ and $\Theta \cap \Theta_{-\delta \boldsymbol{p}}$, depending on the case and the SSI considered. The SSI are expressed on the basis of this operator. For illustration, the relative area of excess pollution (RAEP) is an one-point SSI defined from the above operator A_{Ω}^{Q} by letting $Q = D$ and $\Omega = \Theta$, i.e.,

$$RAEP(\zeta) = A_{\Theta}^{D}[1] = |D|^{-1} \int_{\Theta} d\boldsymbol{p},$$

which varies between 0 (when $\Theta \equiv 0$) and 1 (when $\Theta \equiv D$).

Interpretatively, the RAEP measures the areal fraction of the over-polluted sub-region Θ (i.e., the probability that pollution exceeds ζ at a point $\boldsymbol{p}$). The MEP (also defined in Fig 2b) is a one-point indicator that denotes the mean of the nutrient pollutant concentrations at the threshold (ζ)-exceeding points of the region D (i.e., the mean over-polluting concentration over D). MEDP is the mean difference between the pollutant concentration and ζ at the same points. And, CMEP measures the mean difference between the pollutant concentration and ζ conditioned on the event that the pollutant concentration exceeds ζ (i.e., the focus of CMEP is on points of Θ rather than of D) Clearly, the MEP, MEDP and CMEP are physical one-point indicators of over-pollution (i.e., they refer to various averages of ζ-exceeding pollutant concentrations, with units in *mg*/*L*), whereas the RAEP is a topologic indicator of over-pollution (i.e., it denotes the ζ-exceeding areal fraction, and is unitless). Regarding the relationships between the one-point physical indicators, it is valid that

$$CMEP(\zeta) \geq MEP(\zeta) \geq MEDP(\zeta)$$

where the equalities hold if the entire region is over-polluted, i.e., $|\Theta| = |D|$.

Among the two-point indicators, the non-centered indicator covariance (NIC, see Fig 2c) is a two-point SSI defined by letting $Q = D$ and $\Omega = \Theta \cap \Theta_{-\delta \boldsymbol{p}}$, ($\Theta_{-\delta \boldsymbol{p}}$ denotes the over-polluted Θ sub-region translated by $-\delta \boldsymbol{p}$), i.e.,

$$NIC(\delta \boldsymbol{p}, \zeta) = |D|^{-1} \int_{\Theta \cap \Theta_{-\delta \boldsymbol{p}}} d\boldsymbol{p}.$$

Interpretatively, the NIC measures the connectivity (dependency) between over-polluting concentrations over space-time domain D (i.e., the probability that pollution exceeds ζ at both points $\boldsymbol{p}$ and $\boldsymbol{p}'$ separated by the space-time lag $\delta \boldsymbol{p}$). The PIR (pollution interaction ratio, also defined in Fig 2c) expresses the ratio of the probability that over-pollution occurs at both points $\boldsymbol{p}$ and $\boldsymbol{p} + \Delta \boldsymbol{p}$ divided by the probability that over-pollution occurs at either one of these points. The conditional excess covariance (CEC, Fig 2c) measures the space-time connectivity between nutrient concentrations conditioned by the event that both points belong to the over-polluted sub-region. While NIC and PIR are unitless, the CEC has physical units ((*mg*/*L*)^2).

Interestingly, the SSI are linked to each other by certain functional relationships as shown in Fig 2a. This implies that one can start with the SSI that are the easiest to calculate from the available data, and then conveniently derive all the other SSI from the calculated ones using these relationships. The PIR indicator can be determined in terms of the RAEP and NIC indicators as

$$PIR = \frac{NIC}{2RAEP - NIC}.$$

For numerical, if $PIR = 1$, then $RAEP = NIC$, i.e., the over-pollution two-point connectivity is equal to the over-pollution area ratio. Another two-point indicator, the centered indicator covariance (CIC, Fig 2a), is directly obtained via the relationship

$$CIC = NIC - RAEP^2.$$

The CIC is a two-point indicator that measures how far from independency a pair of ζ-exceeding pollutant concentrations across space-time are (i.e., in a sense it measures the relative strength of spatiotemporal connectivity compared to space-time independency. As such, the larger the CIC is, the farther the pollutant values at points $\boldsymbol{p}$ and $\boldsymbol{p} + \Delta \boldsymbol{p}$ are from being independent.

© 2019 American Geophysical Union. All rights reserved.

In a similar manner, an interesting feature of the SSI theory is that new and useful quantities can be developed on the basis of the standard SSI, depending on the study objectives. For illustration, the indicator variogram (IV, Fig 2a) is defined as the difference

$$IV = RAEP - NIC,$$

which is interpreted as the difference (unitless) between the probability that pollution exceeds ζ at $\boldsymbol{p}$ and the probability that pollution exceeds ζ at both $\boldsymbol{p}$ and $\boldsymbol{p}'$. And, the over-polluting connectivity odds (OCO, Fig 2a) is defined as

$$OCO = \frac{NIC}{1-2RAEP+NIC},$$

which is a useful two-point indicator (unitless) when one wants to compare ζ-exceeding and non ζ-exceeding pollution probabilities between pairs of space-time points. Notice that if $OCO = 0$, then $NIC = 0$ (i.e., zero over-pollution connectivity); and if $OCO = 1$, then $RAEP = \frac{1}{2}$ (i.e., the over-polluted sub-area is half the entire area). For all the above reasons, the setup summarized in Figs 2a-c can be very useful in the efficient calculation of the SSI in practice. We will provide more details on the physical interpretation of the SSI in the context of the study of nutrient pollutants in China's near Seas, see next.

3. Results

3.1 Descriptive statistics and spatial mapping

The descriptive statistics of nitrate and phosphate concentration data are displayed in Table 1. According to the China seawater quality regulations (GB 3097-1997, http://www.sac.gov.cn/), the 4th grade water quality standard (indicating poor quality seawater, Table 2) values for nitrate and phosphate are 0.5 and 0.045 *mg/L*, respectively. The maximum nitrate concentrations were calculated as 4.008, 0.981, 4.216, 2.522 *mg/L* at the BS, YS, ECS and SCS, respectively. Clearly, in the BS, ECS and SCS the nitrate concentrations were found to be 5 to more than 8 times larger than the standard value (0.5 *mg/L*), whereas in the YS the nitrate concentration was almost double the standard value. And, the maximum phosphate concentrations were found to be 0.157, 0.109, 0.307 and 0.1660 *mg/L*, which are all much larger than the standard value (0.045 *mg/L*). Overall, the sampled nitrate and phosphate concentrations were in the range of 0.001-4.216 *mg/L* and 0.0001-0.3079 *mg/L*, respectively; and, we noticed that the ECS, in particular, experienced the highest variation of nitrate and phosphate concentrations.

The nitrate and phosphate concentration maps generated by the BME method are plotted in Fig 3 (using the SEKS-GUI software). The empirical covariance values and fitted space-time covariance models are both presented in Fig S3 of the Supplementary Information (S.I.). From the annual average pollution maps (left of Fig 3), we visually concluded that the nitrate and phosphate distributions exhibit similar spatial patterns. This was supported quantitatively by the *q*-statistic value (=0.71) measuring the spatial correlation of the nitrate and phosphate distributions (the *q*-statistic was calculated using the *Geodetector* software, see http://www.geodetector.org/; Wang et al 2010, 2016; and Text S3 of the S.I.). Moreover, based on these maps, it was found that higher pollution levels emerge in the middle of China around the Yangtze and Qiantang river estuaries, the nitrate and phosphate concentrations were much lower in the seawater of Bohai Rim and South China Sea, whereas light pollution was found in the Liaohe and Pearl river estuaries, and, nitrate and phosphate concentrations exhibited a globally decreasing trend from the estuaries toward the open sea.

The maps at selected times (right of Fig 3) show that the nitrate concentrations were much higher in March (during the cold season, the mean nitrate concentrations were equal to 0.288 and 0.772 at the Bohai Rim and the Yangtze River delta, respectively) than during August (during the warm season, the mean concentrations were equal to 0.185 and 0.572at the Bohai Rim and the Yangtze River delta, respectively). This was more obvious in the Liaohe river and Yangtze river estuaries, whereas the Pearl River estuary shows a different pattern. Higher phosphate concentrations occurred during October, especially at the Liaohe river estuary. The extent of phosphate pollution was geographically much wider along the coastal region of the ECS. Overall, the nutrient pollution of the coastal waters

© 2019 American Geophysical Union. All rights reserved.

in the four China Seas (BS, YS, ECS and SCS) was dominated by the major rivers (e.g., Yangtze and Pearl rivers).

These pollutants mainly come from terrestrial agriculture activities, as well as domestic and industrial sewages (Wang et al. 2018; Wang et al. 2019; Yu et al. 2019). Fig 4 presents monthly variations of nitrate and phosphate concentrations at the selected regions indicated in Fig 3. The Yangtze river delta was the most polluted region for each month. Nitrate and phosphate concentration peaks were observed during March, April, October and November. River discharge dominated the global distribution of nutrient pollution (Qu et al. 2010; Liu et al. 2015). Nutrient concentration is lower in the summer, when there is higher precipitation. Generally, higher precipitation will bring more terrestrial attributes to the sea, whereas in the present case study nutrient concentrations seem to be negatively coordinated with river discharge, this phenomenon (lower nutrient concentration during summer) may be partly due to the dilutive effect (higher precipitation run-off occurred during June, July and August in China), and higher precipitation induced by climate change is expected to increase the riverine total nutrient loading in the future (Sinha et al. 2017). Although nitrate and phosphate concentrations exhibited similar global distributions, they varied locally from one geographic region to another and during different seasons, which suggests that distinct remediation strategies are needed to adequately satisfy the required seawater quality standards.

3.2 Calculation of SSI for nitrate and phosphate concentrations

3.2.1 *One-point SSI*

Based on the BME-generated space-time predictions of nitrate and phosphate concentrations, a set of SSI was calculated that offered additional information to be used in pollution risk assessment. This set includes one-point (i.e., local) indicators (REAP, MEP, MEDP and CMEP) and two-point (i.e., non-local) indicators (NIC, CEC and PIR).

As noted above, the MEP, MEDP and CMEP are physical indicators of over-pollution, whereas the RAEP is a topologic indicator of over-pollution. Accordingly, the plots of Fig 5 illustrate how the physical indicators change as functions of the areal indicator. The RAEP, MEP, MEDP and CMEP denote, respectively, the areal fraction of the over-polluted region, the mean over-polluting nutrient concentration, the mean of the part of the nutrient concentrations that exceeds the threshold, and the nutrient pollutant mean conditioned by the over-pollution condition (as noted earlier, given the values of a small set of these indicators, the corresponding values of the remaining indicators can be conveniently found from them). Let us consider some worth-noticing particular cases (*A*, *B* and *C* correspond to the indicated points in Fig 5):

(*A*) When the nitrate and phosphate threshold values are equal to 0.5 and 0.045 *mg*/*L*, respectively, the corresponding RAEP values are equal to 0.11 and 0.026, respectively. The physical interpretation of these results is that in about 11% and 2.6% of the space-time domain of interest the nitrate and phosphate concentrations, respectively, are higher than the corresponding 4th grade seawater quality standards.

(*B*) For RAEP=0.5, the nitrate and phosphate thresholds are 0.205 and 0.013 *mg/L*, respectively, indicating that during 2015 in China's near Seas about half of the nitrate and phosphate concentrations were higher than 0.205 and 0.013 *mg/L*, respectively.

(*C*) For RAEP=1, the CMEP, MEP and MEDP indicators have in practice the same value over the entire space-time study domain *D* (as is anticipated by the SSI theory).

Fig 5 shows that the MEP and MEDP share the same range of values, i.e., between 0 and the mean nitrate and phosphate concentrations 0.271 and 0.015 *mg/L*, respectively. MEP offers a global assessment of the expected nutrient over-pollution (i.e., exceeding the specified threshold) in a fraction Θ of the domain *D*, whereas MEDP measures the difference between excess $NP(\boldsymbol{p})$ concentrations and the ζ-threshold averaged over *D.* As it can be seen, CMEP $\geq$ MEP $\geq$ MEDP, which was expected in theory. The double equality CMEP=MEP=MEDP holds if RAEP=1 (i.e., the entire region is over-polluted or a zero threshold is assumed); moreover, the equality MEP=MEDP also holds if RAEP=0 (i.e., there is no over-pollution or the threshold is very large). By comparing the

© 2019 American Geophysical Union. All rights reserved.

rates of the decreasing physical MEDP and regional RAEP values with increasing ζ values (see, Fig S4), we concluded that the differential nutrient concentrations over the polluted regional fraction of China's near Seas decrease faster than the polluted regional fraction itself; and that MEDP reaches a zero value at a high threshold value (about 2.2 and 0.05 *mg*/*L* for nitrate and phosphate, respectively). CMEP measures the average of over-polluting nutrient concentrations (i.e., at points within the over-polluted sub-region Θ). The CMEP of both nutrients increase almost linearly as threshold increases, which implies that this indicator can detect the existence of highly polluted areas along China's near Seas. Based on MEDP, another useful indicator, the coefficient of indicator dispersion (CID) can be calculated as

$$CID = \frac{\overline{MEDP(\zeta)}}{\overline{NP(\boldsymbol{p})}},$$

which measures the ratio of over-pollution dispersion normalized by the mean pollution throughout the entire domain of interest. In this study, CID was found to be equal to 0.007 and 0.0001 for the nitrate and phosphate pollution, respectively. The physical meaning of these values is that the average threshold-exceeding nitrate and phosphate concentrations are a small percentage of the corresponding mean pollutant values.

3.2.2 *Two-point SSI*

Selected two-point indicators, i.e., the NIC, CEC and PIR indicators introduced earlier (Fig 2 and Table S1), are plotted in Figs 6 and 7 for specific nutrient (nitrate or phosphate) threshold ζ values. As noted above, the NIC in Fig 6 is a measure of nutrient over-polluting connectivity between points separated by the space-time lag $\delta\boldsymbol{p} = (\delta\boldsymbol{s}, \delta t)$, where $\delta\boldsymbol{s}$ is the spatial lag (distance) and δt is the time lag (separation). Nutrient connectivity can be also interpreted as the probability that pollution exceeds ζ at both points $\boldsymbol{p}$ and $\boldsymbol{p}'$ separated by $\delta\boldsymbol{p}$. The CEC indicator measures the space-time connectivity between nutrient concentrations conditioned by the over-polluted points. The PIR indicator measures the co-variation strength of joint over-pollution incidences at points $\boldsymbol{p}$ and $\boldsymbol{p}'$ *vs*. the alternate case that over-pollution occurs at either one of these points. That is, PIR may be interpreted as the ratio of the probability that nutrient concentrations exceed a threshold at both space-time points $\boldsymbol{p}$ and $\boldsymbol{p}'$ over the probability that nutrient concentrations exceed the threshold at either $\boldsymbol{p}$ or $\boldsymbol{p}'$).

Visually, the NIC, CEC and PIR plots in Figs 6 and 7 are surfaces that vary with the space-time lag $\delta\boldsymbol{p}$. It is worth-noting that the NIC and PIR surfaces decrease with increasing ζ, whereas the CEC surface increases with increasing ζ. The physical meaning of this behavior is that spatiotemporal nutrient connectivity increases as a function of ζ, but the relative strength of this connectivity compared to independency decreases with ζ. We also observe that for the nitrate and phosphate pollutants, the NIC values are higher for smaller ζ thresholds, which indicates that higher connectivity exists between nitrate or phosphate concentrations exceeding these ζ values at both points $\boldsymbol{p}$ and $\boldsymbol{p}'$. As is shown in Figs 6 and 7, the PIR decreases as the threshold ζ increases, and the drop rate was faster at smaller spatial distances and time separations, indicating that high nutrient pollutant concentrations were rather clustered.

For numerical illustration, if the nitrate threshold values are ζ =0.2 and 0.5 *mg*/*L*, the corresponding NIC values are 0.41 and 0.06, respectively (Fig 6), indicating that 41% and 6% of the point pairs separated by $\delta\boldsymbol{p} = (\delta\boldsymbol{s}, \delta t)$ within the domain of interest *D* (i.e., China's near Seas during 2015) exceeded the 1st and 4th grades seawater quality standards (GB 3097-1997, http://www.sac.gov.cn/, Table 2). Also, at the same spatial distance $\delta\boldsymbol{s}$ and time separation δt, the nitrate NIC decreases faster for a small threshold than for a large one, i.e., the NIC experiences a steeper decline. For numerical illustration, for ζ=0.2 *mg*/*L* the nitrate NIC ranges from 0.49 to 0.35 and the decreasing rate was higher than for ζ=0.5 *mg*/*L*, when the NIC ranges from 0.094 to 0.034. This indicates that the nitrate NIC values were more clustered for larger than for smaller ζ values. Regarding phosphate pollution, if the threshold values are ζ =0.015 and 0.045 *mg*/*L*, the corresponding NIC values were 0.346 and 0.007, respectively (Fig 7), indicating that 34.6% and 0.7%

© 2019 American Geophysical Union. All rights reserved.

of the point pairs separated by $\delta \boldsymbol{p}$ within the domain of interest exceeded the 1st and 4th grades seawater quality standards. The CEC values for nitrate and phosphate showed a large variation at different space-time lags (Figs 6 and 7). Peaks and valleys were observed at certain lags, e.g., peaks were observed at the spatial distance $\delta s = 150$ *km* and temporal separations $\delta t = 2$ and 4 *months*, whereas valleys were observed at the distance $\delta s = 50$ *km* and separations $\delta t = 2$ and 4 *months*. These observations regarding the CEC behavior can help explain the seasonal changes and fluctuations of nutrient concentrations and their space-time connectivity variations, thus providing useful information about the locations of extremely polluted area and the occurrences of pollution events.

4. Discussion-Conclusions

The nitrate and phosphate concentrations showed similar overall distributions throughout the space-time domain of interest, i.e., along China's near Seas during the year 2015. Extremely high concentrations were observed at the Yangtze river, Pearl river and Liaohe river estuaries. Nitrate pollution was much more serious than phosphate pollution, with 11% of individual domain points (based on RAEP calculations) and 6% of joint domain points (based on NIC calculations) exceeding the 4th grade seawater quality standard. It was found that the annual space-time average nitrate and phosphate concentrations were 0.271 and 0.015 *mg*/*L*, respectively. The temporal nitrate and phosphate patterns exhibited certain differences including the emergence of seasonally high values. Hence, incorporating key dynamics (e.g., temporal variations) in future investigations is necessary for an adequate nutrient pollution modeling and mapping in the space-time domain of interest, and the same is true regarding the local marine environment and seasonal human activities.

4.1 BME implementation

The BME method was employed to model composite space-time nutrient pollutant spread and predict nitrate and phosphate concentrations at unmonitored locations and times by incorporating, in a composite manner, both spatial and temporal pollutant variations. Unlike traditional Kriging and similar techniques, BME makes no restrictive assumptions concerning the linearity of the predictor and the Gaussian (normal) probability distribution of the samples, i.e., non-linear predictors and non-Gaussian distributions are generally assumed that are more realistic model features that can better depict the in situ variations of nutrient pollutant concentrations. Based on a limited set of samples along China's near Seas obtained during 2015, BME provided a probabilistically complete characterization of the space-time nutrient pollutant distributions and generated pollutant concentration predictions that accounted for both spatial and temporal pollutant correlations and cross-dependencies.

Regarding the BME implementation, as has been shown in several previous studies (e.g., Lee et al. 2008; Yu et al. 2009; Gao et al. 2014; Jiang et al. 2019), BME can provide more accurate attribute estimates than the mainstream geostatistical techniques for space-time analysis and SSI assessment purposes; it can produce useful information based on limited datasets; it is easily implemented and cost-effective compared to other numerical modeling techniques; and, it has the distinctive ability to assimilate various types of environmental information, both core and site-specific. Accordingly, given its successes in other scientific fields, the potential usefulness of BME modeling in Oceanography deserves serious consideration (e.g., ocean models, considered as core knowledge in the BME framework, can be combined with remote sensing data, considered as site-specific data, to improve the large-scale prediction accuracy of ocean attributes).

For the BME implementation in practice to function optimally, the availability of sufficient input information is needed. With this in mind, in the present study, the pollutant prediction accuracy was affected by two main factors: (*a*) The first factor is that, in general, BME is sensitive to the distribution and density of the available nutrient concentration samples (this is, also, valid for other prediction techniques). Monthly samples were mostly collected during March, May, August and October, whereas considerable uncertainty characterized the estimation of nutrient concentrations during other months and, as a consequence, the global temporal trend analysis. And, the high temporal variability and low temporal correlation of nutrient concentrations can also affect the monthly prediction accuracy. (*b*) The second factor is that coastal waters are heavily affected by land-sea

© 2019 American Geophysical Union. All rights reserved.

interactions, and considerable differences in pollution status may exist at a small scale (both spatial and temporal) under different marine hydrodynamics and biogeochemical conditions (Khangaonkar et al. 2018; Ren et al. 2016). Yet, even under these limitations of input information, it was found that BME performed well.

As regards future research, and in light of the above considerations, frequent in-situ temporal monitoring is suggested to enable the development of a robust space-time model of nutrient distributions. Also, the incorporation of informative environmental data and ocean physical laws in to BME modeling can reduce uncertainties and generate better pollutant predictions (Lang and Christakos 2018).

4.2 SSI implementation

Nutrient loading and spread can vary significantly over short distances and during different time periods, and the space-time pollutant distributions are often characterized by non-negligible in-situ uncertainties. SSI analysis offered a rigorous quantitative nutrient pollution assessment that accounted for both the natural variabilities (at a local and a global scale) as well as the uncertainty sources of the pollution phenomenon. The physical interpretations of the quantitative results of the SSI analysis can improve the understanding of the pollution phenomenon along China's near Seas during 2015. For example, the NIC indicators of the nitrate and phosphate concentrations both decrease as functions of the spatial and temporal lags, with the spatial decline being larger than the temporal one. The physical meaning of the NIC behavior is that the actual nitrate and phosphate distributions exhibit similar spatial clusters over China's near Seas. We notice that when temporal dynamics are considered, the clustered trend was not so obvious in the pollutant time series. As regards the CEC indicator, its range of variation was larger and its declining trend was more distinct when high threshold ζ values were considered (e.g., the width of the nitrate CEC range was about 0.4 $(mg/L)^2$ when $\zeta = 0.5$ mg/L, but only 0.04 when $\zeta = 0.2$ mg/L), which indicates that higher CEC values were clustered locally in specific areas of China's near Seas. Also, it was found (Figs 6 and 7) that the spatial correlation range was about 140km for nitrate and 80-100km for phosphate. Physically, this means that the actual nitrate distribution was more dispersed geographically than the phosphate distribution. Such useful space-time information gained by SSI analysis can guide pollution management and facilitate effective policy-making.

Overall, the one- and two-point SSI have been shown to be useful tools that can improve the quantitative description of seawater pollution across space-time. Although the nutrient dataset considered in this study was collected during a single year (2015), the SSI analysis of nutrient datasets obtained during multiple years can be considered, when available. This means that a more detailed and long-term seawater data quality monitoring is needed to get a more comprehensive understanding of the evolution of annual nutrient pollutant variations along China's near Seas.

4.3 Nutrient Pollution in China and Relevant Pollution Management Issues

Following China's reform and opening-up policy initiative of 1978, water quality problems became much more serious as a result of the increasing population, rapid agriculture development and urbanization (Wang et al. 2018, Yu et al. 2019). Extreme nutrient pollution can be observed in most of China's estuaries (Fig 3), and terrestrial inputs are still the most important external sources of nutrients (nitrate, N, and phosphate, P) in coastal waters. Controlling both N and P loadings from upstream is believed to be a reliable management strategy of restoring seawater quality along the entire freshwater-marine continuum (Conley et al. 2009; Paerl et al. 2009, 2018). In terms of the RAEP indicator, we found that a high nitrate or phosphate threshold value (point A in Figs 5a and b) lies on the cusp of a steep RAEP increase, which is very important from a management perspective. Indeed, this information indicates that a relatively small increase in the quantity of nitrogen introduced in to the system could lead to a large increase in the regional area that exceeds the 4th grade seawater quality standards. The sensitivity of these coastal conditions is also reinforced when looking at the impacts of small nitrate threshold reductions. The RAEP for a nitrate threshold of 0.4 mg/L (3rd grade seawater quality standard) is 0.2, which implies an increase of about 9% of the threshold exceeding area compared to the 4th grade seawater quality standard. The corresponding conditions for

© 2019 American Geophysical Union. All rights reserved.

phosphate concentrations are not as sensitive. Indeed, the RAEP for a phosphate threshold of 0.03 *mg*/*L* (3rd grade seawater quality standard) is about 0.096 which implies an increase of about 7% of the threshold exceeding area. The RAEP indicator can also determine the pollution remediation area for cost evaluation purposes. And, if it is assumed that the remediation target and remediation cost are linked by a linear relationship (i.e., lower remediation target and higher N or P concentrations need more remediation cost), the MEDP indicator (average difference between excess N or P concentration *vs*. the specified threshold, i.e., the difference between current pollution level and remediation target) could express the remediation cost.

Adequate long-term seawater quality monitoring data is still in high demand for improving the scientific characterization and assessment of nutrient pollution in China. In turn, comprehensive characterization and assessment are fundamental prerequisites for identifying those suitable management interventions that can recover a degraded marine ecosystem in coastal waters. And, further quantitative analysis of nutrient thresholds and their evolution can support the restoration of safe and sustainable nutrient levels in the environmentally heterogeneous China's near Seas. Lastly, considered in synergy, the proposed BME and SSI approaches can be useful to researchers and practitioners seeking an adequate assessment of marine environmental impacts, which is a prerequisite of effective remediation policy-making.

Acknowledgments

This research work was supported by a grant by the National Natural Science Foundation of China (Grant NSFC 41606124 & 41671399). We thank the State Oceanic Administration for providing seawater quality data. Details about data sources are presented in supporting information.

References

Breitburg, D., Levin, L. A., Oschlies, A., Grégoire, M., Chavez, F. P., Conley, D. J., et al. (2018). Declining oxygen in the global ocean and coastal waters. Science, 359(6371), eaam7240

Christakos G., (1990). A Bayesian/maximum-entropy view to the spatial estimation problem. 1990. Math. Geol. 22 (7), 763−777

Christakos G., Hristopulos D.T., (1996a). Characterization of atmospheric pollution by means of stochastic indicator parameters. Atmos. Environ. 30 (22), 3811−3823

Christakos G., Hristopulos D.T., (1996b). Stochastic indicators for waste site characterization. Water Resour. Res. 32 (8), 2563–2578

Christakos G., (2000). Modern Spatiotemporal Geostatistics. Oxford University Press, New York.

Christakos G., (2017). Spatiotemporal Random Fields: Theory and Applications. Elsevier, Amsterdam, the Netherlands

Cai W, Hu X, Huang W, Murrell MC, Lehrter JC, Lohrenz SE et al. (2011). Acidification of subsurface coastal waters enhanced by eutrophication. Nature Geoscience, 4(11), 766–770

Conley D.J., Paerl H.W., Howarth R.W., Boesch D.F., Seitzinger S.P., Havens, K. E., Lancelot C., Likens G.E. (2009). Ecology. controlling eutrophication: nitrogen and phosphorus. Science, 323(5917), 1014

Coulliette, A.D., Money, E.S., Serre, M.L., & Noble, R.T. (2009). Space/time analysis of fecal pollution and rainfall in an eastern north carolina estuary. Environmental Science & Technology, 43(10), 3728-3735

Diaz, R.J. and Rosenberg, R., (2008). Spreading Dead Zones and Consequences for Marine Ecosystems. Science, 321, 926-929

Everaert, G., Ruus, A., DØ Hjermann, K Borgå, Green, N., Boitsov, S., Jensen H., Poste A. (2017). Additive models reveal sources of metals and organic pollutants in Norwegian marine sediments. Environmental Science & Technology, 51(21)

Fei, X., Christakos, G., Lou, Z., Ren, Y., Liu, Q., Wu, J. (2016). Spatiotemporal co-existence of female thyroid and breast cancers in Hangzhou, China. Scientific Report, 6(1), 28524

Gao S, Zhu Z, Liu S, Jin R, Yang G, Tan L (2014) Estimating the spatial distribution of soil moisture based on Bayesian maximum entropy method with auxiliary data from remote sensing. Int J Appl Earth Obs Geoinf 32:54–66

Howarth, RW, Marino R. (2006). Nitrogen as the limiting nutrient for eutrophication in coastal marine ecosystems: Evolving views over three decades. Limnology & Oceanography, 51: 364-376

Huang, J. , Li, Q. , Huang, L. , Zhang, Z. , Mu, J. , & Huang, Y. . (2013). Watershed-scale evaluation for land-based nonpoint source nutrients management in the bohai sea bay, china. Ocean & Coastal Management, 71, 314-325

© 2019 American Geophysical Union. All rights reserved.

He, J., & Kolovos, A. (2018). Bayesian maximum entropy approach and its applications: a review. Stochastic Environmental Research and Risk Assessment, 32(4), 859-877
He, J., Yang, Y., Christakos, G., Liu, Y., & Yang, X. (2019). Assessment of soil heavy metal pollution using stochastic site indicators. Geoderma, 337, 359-367
Jiang, Q., He, J., Wu, J., Hu, X., Ye, G., & Christakos, G. (2019). Assessing the severe eutrophication status and spatial trend in the coastal waters of Zhejiang province (China). Limnology and Oceanography, 64(1), 3-17
Jiang, Q., He, J., Ye, G., & Christakos, G. (2018). Heavy metal contamination assessment of surface sediments of the East Zhejiang coastal area during 2012–2015. Ecotoxicology and environmental safety, 163, 444-455
Kitsiou, D., & Karydis, M.. (2011). Coastal marine eutrophication assessment: a review on data analysis. Environment International, 37(4), 0-801
Khangaonkar, T., Nugraha, A., Xu, W., Long, W., Bianucci, L., Ahmed, A., ... & Pelletier, G. (2018). Analysis of hypoxia and sensitivity to nutrient pollution in Salish Sea. Journal of Geophysical Research: Oceans, 123(7), 4735-4761.
Lee S-J, Balling R, Gober P (2008). Bayesian maximum entropy mapping and the soft data problem in urban climate research. Ann Assoc Am Geogr 98:309–322
Lundberg C, Jakobsson BM, Bonsdorff E. (2009). The spreading of eutrophication in the eastern coast of the Gulf of Bothnia, northern Baltic Sea - an analysis in time and space. Estuar Coast Shelf 82:152-160
Li, H. M. , Tang, H. J. , Shi, X. Y. , Zhang, C. S. , & Wang, X. L. . (2014). Increased nutrient loads from the changjiang (yangtze) river have led to increased harmful algal blooms. Harmful Algae, 39, 92-101
Liu, K. K. , Yan, W. J. , Lee, H. J. , Chao, S. Y. , Gong, G. C. , & Yeh, T. Y. . (2015). Impacts of increasing dissolved inorganic nitrogen discharged from changjiang on primary production and seafloor oxygen demand in the east china sea from 1970 to 2002. Journal of Marine Systems, 141(141), 200-217.
Lang, Y., & Christakos, G. (2018). Ocean pollution assessment by integrating physical law and site‐specific data. Environmetrics, DOI: 10.1002/env.2547
Murphy, R. R., Curriero, F. C., & Ball, W. P.. (2010). Comparison of spatial interpolation methods for water quality evaluation in the chesapeake bay. Journal of Environmental Engineering, 136(2), 160-171
Paerl, H. W. (2009). Controlling eutrophication along the freshwater–marine continuum: dual nutrient (n and p) reductions are essential. Estuaries & Coasts, 32(4), 593-601
Paerl, H. W. , Otten, T. G. , & Kudela, R. . (2018). Mitigating the expansion of harmful algal blooms across the freshwater-to-marine continuum. Environmental Science and Technology, 52(10). DOI: 10.1021/acs.est.7b05950
Primpas,I., Tsirtsis, G., Karydis, M., & Kokkoris, G.D. (2010). Principal component analysis: Development of a multivariate index for assessing eutrophication according to the European water framework directive. Ecological Indicators, 10(2), 178-183
Qu, H.J., & Kroeze, C. (2010). Past and future trends in nutrients export by rivers to the coastal waters of China. Science of the Total Environment, 408(9), 2075-2086
Ren, J., Gao, B.B., Fan, H.M., Zhang, Z.H., Zhang, Y., Wang, J.F. (2016). Assessment of pollutant mean concentrations in the yangtze estuary based on msn theory. Marine Pollution Bulletin,113, 216-223.
Smith, VH. (2006). Responses of estuarine and coastal marine phytoplankton to nitrogen and phosphorus enrichment. Limnology & Oceanography, 51(1part2), 377-384
Strokal, M., Yang, H., Zhang, Y., Kroeze, C., Li, L., Luan, S., Wang H., Yang S., Zhang Y. (2014). Increasing eutrophication in the coastal seas of China from 1970 to 2050. Marine Pollution Bulletin, 85(1), 123-140
Sinha, E. , Michalak, A. M. , & Balaji, V (2017). Eutrophication will increase during the 21st century as a result of precipitation changes. Science, 357(6349), 405-408
Wang JF, Zhang TL, Fu BJ (2016). A measure of spatial stratified heterogeneity. Ecological Indicators 67(2016): 250-256
Wang JF, Li XH, Christakos G, Liao YL, Zhang T, Gu X and Zheng XY (2010). Geographical detectors-based health risk assessment and its application in the neural tube defects study of the Heshun region, China. International Journal of Geographical Information Science 24(1): 107-127
Wang B., Xin M., Wei Q., Xie L. (2018). A historical overview of coastal eutrophication in the China seas. .Marine Pollution Bulletin, 136, 394-400
Wang J, Yu Z, Wei Q and Yao Q (2019). Long‐Term Nutrient Variations in the Bohai Sea Over the Past 40 Years. Journal of Geophysical Research: Oceans, 124(1), 703-722.
Yu HL, Kolovos A, Christakos G, Chen JC, Warmerdam S, Dev B. (2007). Interactive spatiotemporal modeling of health systems: the SEKS-GUI framework. Stoch Env Res Risk A 21:555-572
Yu HL, Chen JC, Christakos G, Jerrett M (2009) BME estimation of residential exposure to ambient PM10 and Ozone at multiple time scales. Environ Health Perspect 117:537–544
Yu C, Huang X, Chen H, Godfray HCJ, Wright JS, Hall JW, et al. (2019). Managing nitrogen to restore water quality in China. Nature, 567(7749), 516

© 2019 American Geophysical Union. All rights reserved.

Yang Y, Christakos G. (2015). Spatiotemporal characterization of ambient PM2.5 concentrations in Shandong province (China). Environ Sci Technol 49:13431-13438

Zhou Y, Obenour DR, Scavia D, Johengen TH and Michalak AM (2013). Spatial and temporal trends in lake erie hypoxia, 1987–2007. Environmental Science and Technology, 47(2), 899-905

Accepted Article

© 2019 American Geophysical Union. All rights reserved.

Figure 1: Spatial distribution of sampling sites along China's near Seas (monthly sampling; for illustration, the black dots indicate samples obtained during March of 2015), and the study area boundary (orange line, 12 nautical miles).

© 2019 American Geophysical Union. All rights reserved.

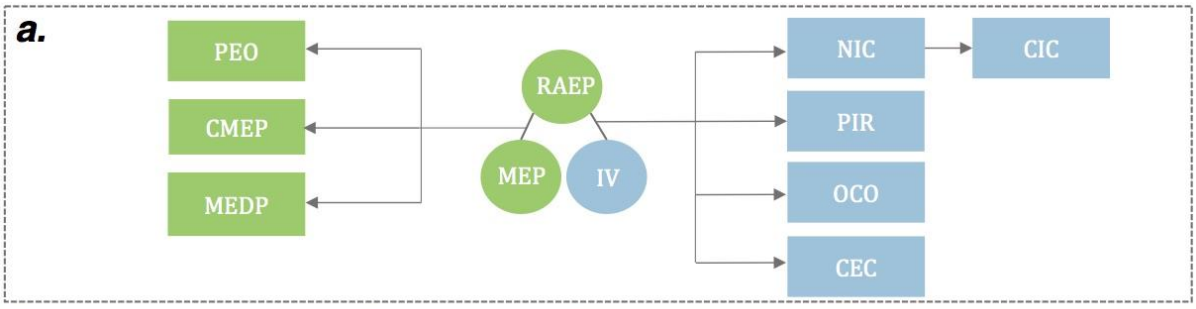

b.

One-point SSI	Definition
RAEP: Relative area of excess pollution	$A^D_\Theta[1]$
MEP: Mean excess pollution	$A^D_\Theta[NP(\boldsymbol{p})]$
MEDP: Mean excess differential pollution	$A^D_\Theta[NP(\boldsymbol{p})-\zeta]$
CMEP: Conditional MEP	$A^\Theta_\Theta[NP(\boldsymbol{p})]$

c.

Two-point SSI	Definition
NIC: Non-centered indicator covariance	$A^D_{\Theta\cap\Theta_{-\delta p}}[1]\ if\ \lvert\delta\boldsymbol{p}\rvert \le d$ $0\qquad if\ \lvert\delta\boldsymbol{p}\rvert \ge d$
CEC: Conditional excess covariance	$A^{\Theta\cap\Theta_{-\delta p}}_{\Theta\cap\Theta_{-\delta p}}[NP(\boldsymbol{p})NP(\boldsymbol{p}+\delta\boldsymbol{p})]$
PIR: Pollution interaction ratio	$\dfrac{A^D_{\Theta\cap\Theta_{-\Delta p}}[1]}{2A^D_\Theta[1]-A^D_{\Theta\cap\Theta_{-\Delta p}}[1]}$

Figure 2: (*a*) Relationships between calculated SSI (circles) and derived SSI (squares), (*b*) definitions of one-point SSI, (*c*) definitions of two-point SSI. More details can be found in the Supporting Information, Table S1.

Accepted Article

© 2019 American Geophysical Union. All rights reserved.

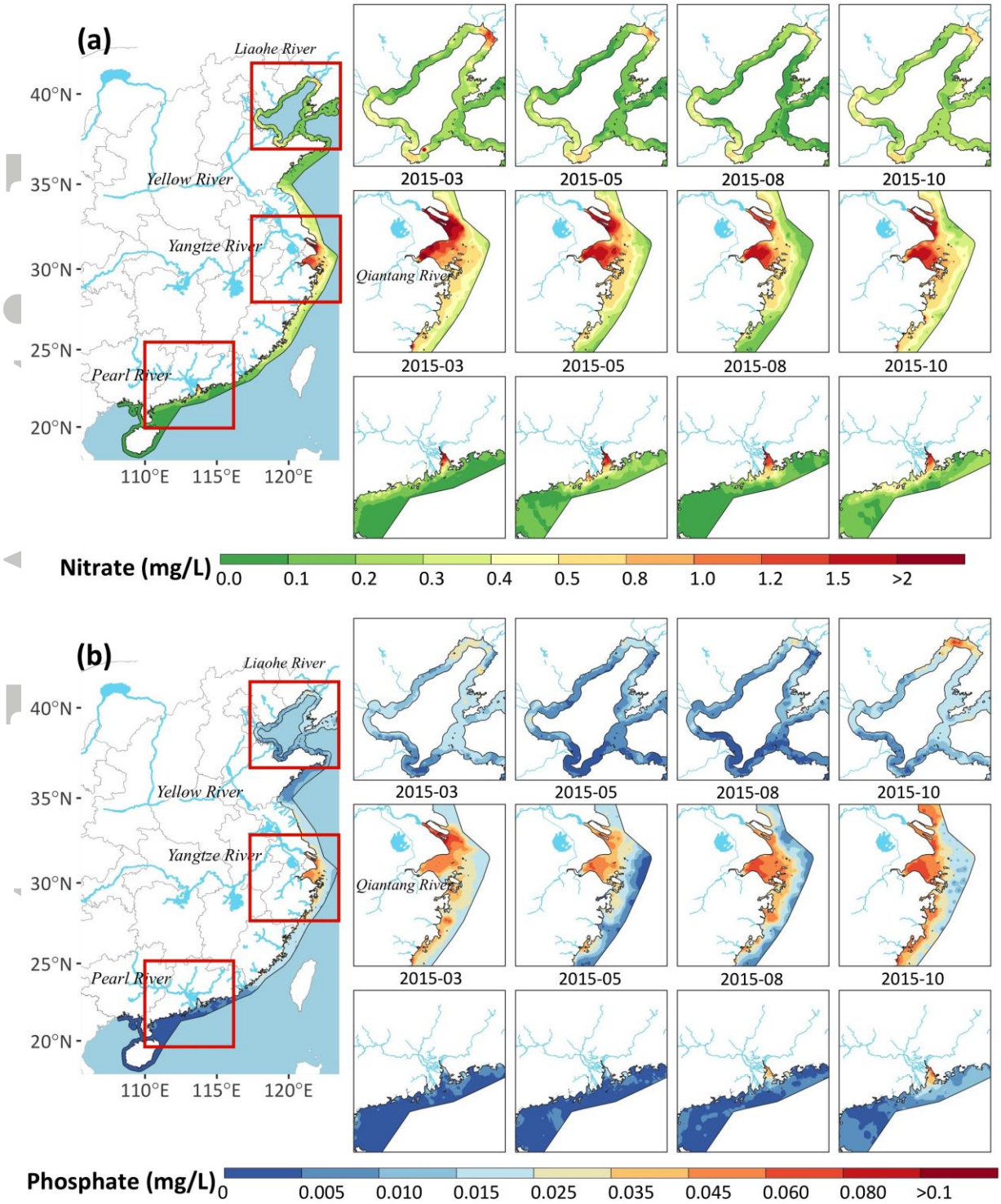

Figure 3: BME-generated spatial maps of (*a*) nitrate and (*b*) phosphate concentrations. In particular, the annually averaged maps are shown on the left, whereas selected monthly maps for the coastal sea sub-regions of Bohai Rim, Yangtze River delta and Pearl River delta (from top to bottom) are shown on the right.

© 2019 American Geophysical Union. All rights reserved.

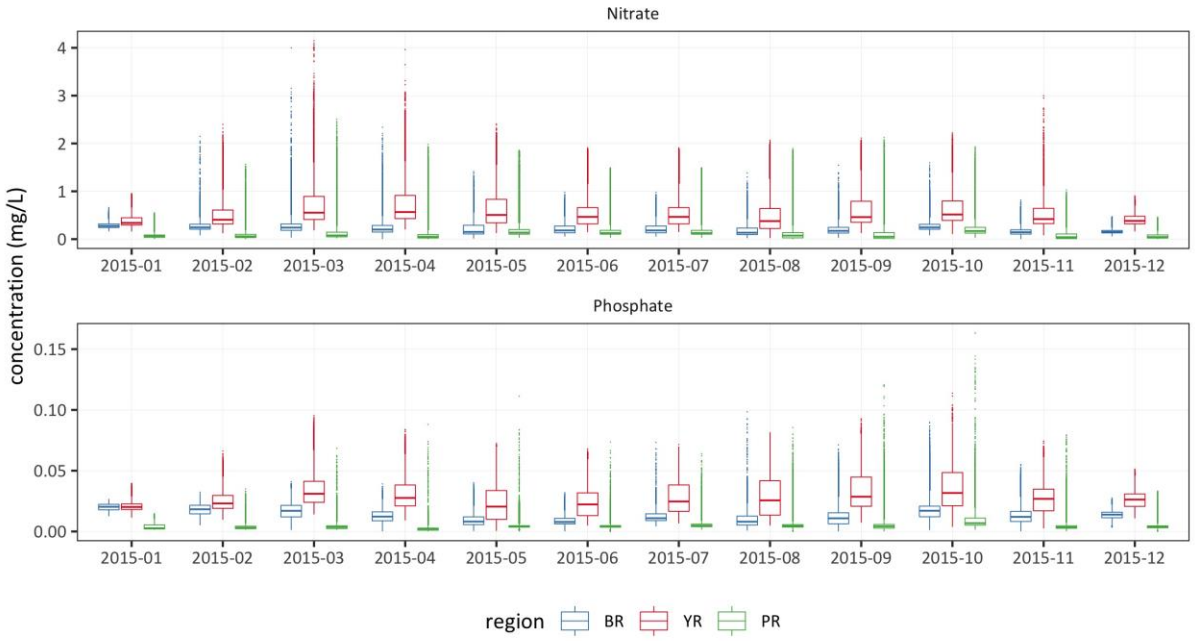

Figure 4: Box-plots of monthly (*a*) nitrate and (*b*) phosphate concentration variations for the selected regions of Bohai Rim (BR, 37368 pixels), Yangtze River delta (YR, 35820 pixels) and Pearl River delta (PR, 30060 pixels) indicated by red squares in Fig 3 during the period 2015-01 to 2015-12 (-01 denotes the month of January, -02 denotes February etc.).

Accepted Article

© 2019 American Geophysical Union. All rights reserved.

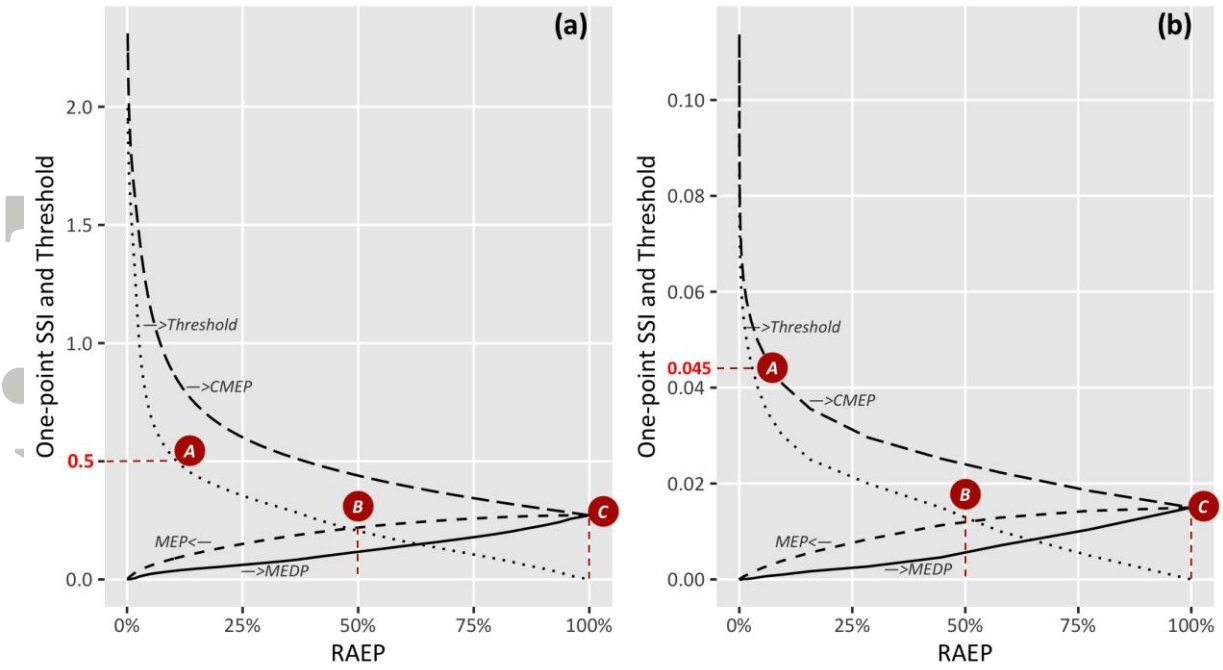

Figure 5: Plots of one-point SSI (CMEP, MEP, MEDP, RAEP) and threshold ζ for (*a*) nitrate and (*b*) phosphate concentration distributions. The red circles indicate the cases of (*A*) the special threshold values $\zeta(nitrate) = 0.5 mg/L$ and $\zeta(phosphate) = 0.045 mg/L$, (*B*) the RAEP=0.5, and (*C*) the RAEP=1.

Accepted

© 2019 American Geophysical Union. All rights reserved.

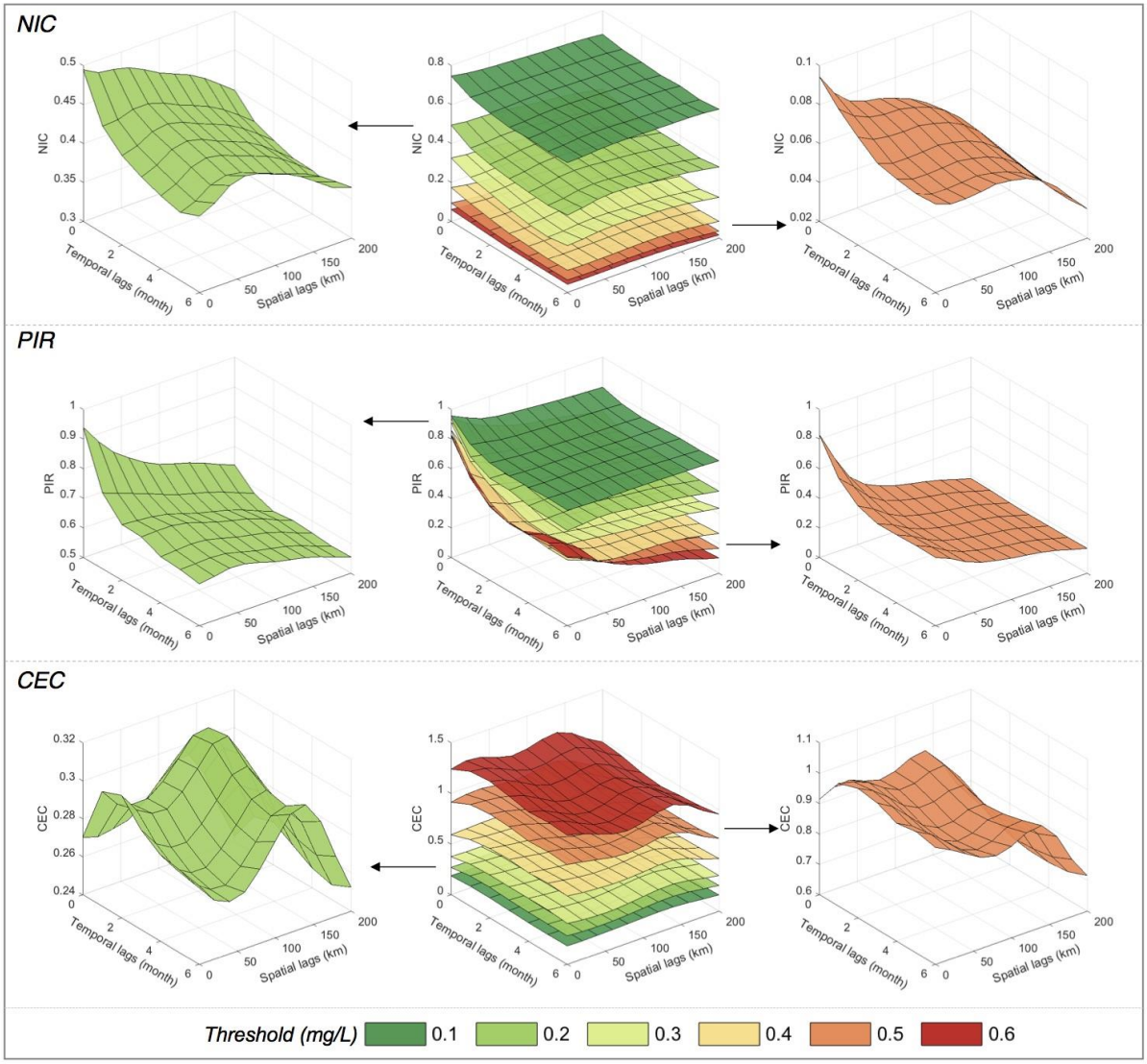

Figure 6: Two-point SSI (NIC, PIR & CEC) plots as functions of the selected nitrate concentrations threshold ζ (0.1, 0.2, 0.3, 0.4, 0.5 and 0.6 *mg/L*) based on space-time BME estimation. Detailed plots for selected thresholds (based on the 1st and 4th grades of seawater quality standards GB 3097-1997, 0.2 and 0.5 *mg/L*, see also Table 2) are shown on the left and right.

Accepted

© 2019 American Geophysical Union. All rights reserved.

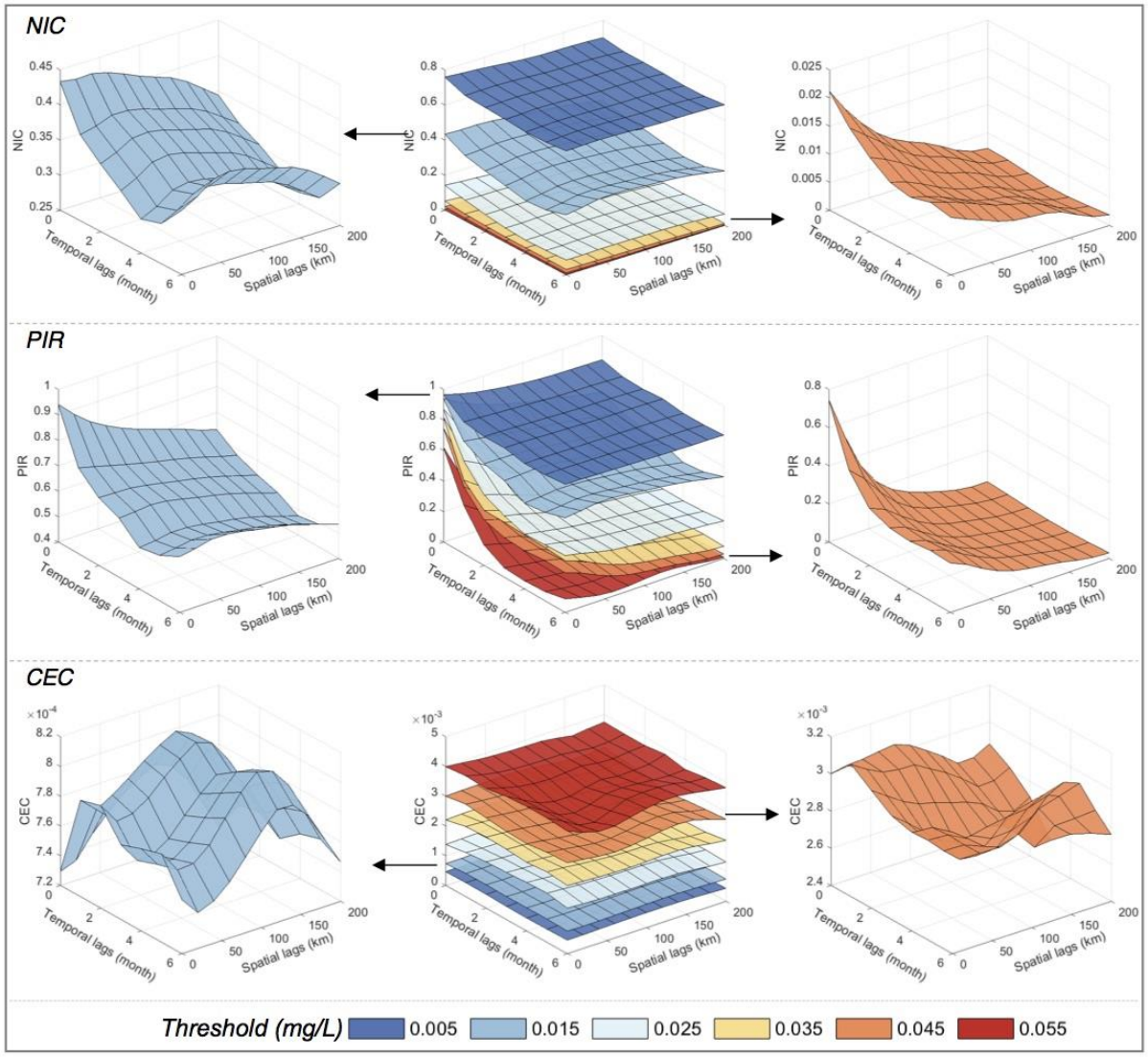

Figure 7: Two-point SSI (NIC, PIR & CEC) plots as functions of the selected phosphate concentrations threshold ζ (0.005, 0.015, 0.025, 0.035, 0.045 and 0.055 mg/L) based on space-time BME estimation; plots for selected thresholds (based on the 1st and 4th grades of seawater quality standards GB 3097-1997, 0.015 and 0.045 *mg/L*, see also Table 2) are on the left and right for details.

Accepted

© 2019 American Geophysical Union. All rights reserved.

Table 1: Summary statistics of samples obtained at Bohai Sea (BS), Yellow Sea (YS), East China Sea (ECS) and South China Sea (SCS) from January to December of 2015.

Region	*Samples*	*Nitrate* (*mg*/*L*)				*Phosphate* (*mg*/*L*)			
		Min	*Max*	*Mean*	*Std dev*	*Min*	*Max*	*Mean*	*Std dev*
BS	652	0.010	4.008	0.299	0.304	0.0006	0.1570	0.0138	0.0127
YS	977	0.001	0.981	0.214	0.198	0.0004	0.1090	0.0137	0.0130
ECS	1187	0.020	4.216	0.703	0.608	0.0001	0.3079	0.0370	0.0263
SCS	1146	0.001	2.522	0.214	0.369	0.0003	0.1660	0.0073	0.0124

Table 2: China's seawater quality standard (GB 3097-1997) for nitrate and phosphate (*mg*/*L*).

Nitrate Less than	*Phosphate Less than*	*Class*	*Suitable for:*
0.2	0.015	I	Marine fishery waters, marine nature reserves etc.
0.3		II	Aquaculture, seawater baths etc.
0.4	0.030	III Slightly polluted	Industrial water use, coastal scenic area.
0.5	0.045	IV Moderately polluted	Sea port waters, marine development zone
		Heavily polluted	

Accepted Article

© 2019 American Geophysical Union. All rights reserved.